Large Mid-Infrared SHG Activities in Eu(II)-Based Quaternary Chalcogenides

Subhendu Jana,[1] Eric A. Gabilondo,[2] Yujie Zhang,[2] P. Shiv Halasyamani,[2] and Paul A. Maggard[1,*]

[1] Department of Chemistry, North Carolina State University, Raleigh, North Carolina, USA, 27695.

[2] Department of Chemistry, University of Houston, Houston, Texas, USA, 77204.

*Corresponding author e-mail: Paul_Maggard@ncsu.edu

Abstract. Complex metal-chalcogenides have received growing attention for second-harmonic generation (SHG) activity arising from their noncentrosymmetric structures. In this area, the impact of the Eu(II)-cation on their structures and optical properties has not been well explored. Synthetic investigations of the Eu-Ag-IV-Ch (IV = Sn or Ge; Ch = S or Se) systems have unveiled four rare examples of Eu(II)-based quaternary chalcogenides exhibiting very large mid-IR SHG responses within the chemically-rich systems $II\text{-}I_2\text{-}IV\text{-}Ch_4$ and $II_3\text{-}I_2\text{-}IV_2\text{-}Ch_8$ (Ch = S or Se; I, II, and IV = monovalent, divalent and tetravalent cations, respectively). Their structures were characterized by single-crystal X-ray diffraction (SCXRD) methods to crystallize in noncentrosymmetric space groups, $I\bar{4}2m$ for $EuAg_2GeS_4$ (**I**) and $I\bar{4}3d$ for $Eu_3Ag_2Ge_2Se_8$ (**II**) $Eu_3Ag_2Sn_2Se_8$ (**III**) and $Eu_3Ag_2Sn_2S_8$ (**IV**). The structures consist of body-centered arrangements of $(Ge/Sn)Ch_4$ tetrahedra that are fully oriented and bridged by flattened $AgCh_4$ tetrahedra into 3D networks and charge-balanced by Eu(II) cations. Their crystalline powders exhibit mid-IR (2.09 μm) SHG responses among the largest reported to date, ranging from a large ~1.9 × AGS ($AgGaS_2$) for **I**, to remarkably high activities of ~30 for **III**, ~70 for **II**, and ~100 for **IV** × AGS. Spin-polarized band structure calculations showed the valence and conduction band edge states stem from

interactions of the Ag-to-S/Se and Ge/Sn-to-S/Se based states, respectively, with increasing contributions of the Eu(II) $4f^7$-based in the order of **I < III < II < IV**. Most interestingly, this trend strongly correlates with the SHG activity, suggesting a potential new strategy for understanding and attaining cutting-edge SHG properties within Eu(II)-based chalcogenides. Thus, these results unveil a deeper understanding of structure-optoelectronic/SHG property relationships.

---

1. Introduction.

Multinary metal chalcogenides have represented some of the most promising compounds for their advanced nonlinear optical (NLO) properties stemming from noncentrosymmetric crystal structures. Materials with NLO properties have wide potential applications, for example, in healthcare,[1] remote sensing,[2] CO_2 detection,[3] and military security.[4] Within this area, metal chalcogenides have demonstrated among the largest second-harmonic generation (SHG) responses and laser induced damage threshold (LIDT) for infrared NLO applications, with $AgGaCh_2$ (Ch = S and Se) and $ZnGeP_2$ serving as benchmark compounds.[5] However, the $AgGaCh_2$ compounds exhibit poor LIDT and $ZnGeP_2$ shows non-negligible optical absorption in the wavelength range of 0.7 to 2 μm. A related compound, γ-$NaAsSe_2$, shows one of the highest known SHG responses (~75 × $AgGaS_2$),[6,7] but is unstable in an ambient atmosphere and undergoes a phase transition to a centrosymmetric polymorph. Prominent challenges for an ideal NLO material include exhibiting a maximal possible SHG response and to remain stable in air, as well as possess a high LIDT and a wide transparency window as compared to commercial $AgGaS_2$.[8-10]

Synthesis of multinary metal chalcogenides has remained an active and longstanding area of research for solid-state scientists across the community because of their rich structural chemistry and for the wide variation and tunability of their physical properties.[11-16] Thus, a prominent strategy for attaining advanced NLO properties has been to synthetically target chemical substitutions within noncentrosymmetric structure types, such as for the chalcopyrite and related diamond-type structures. For example, the incorporation of rare-earth elements into chalcophosphates has been demonstrated to significantly improve the LIDT without

2

sacrificing the SHG response magnitude.[17,18] Additionally, co-substitution of alkali or alkaline earth metals with main-group metal cations such as Sn(IV) and Ge(IV) has been found to increase their bandgaps and inhibit multi-photon absorptions by removing *d-d* or *f-f* transitions.[19] Effective leveraging of these combined strategies was pursued herein in the synthetic exploration of air-stable noncentrosymmetric chalcogenides within the chemically-rich II–I–IV–Ch (II = Ba, Sr, Pb, or Eu; I = Li, Cu or Ag; IV = Si, Ge, or Sn; Ch = S or Se) systems. Prior studies have revealed that compounds in these systems commonly occur with the II–I_2–IV-Ch_4 and II_3–I_2–IV_2–Ch_8 compositions and with noncentrosymmetric, SHG-active, structures. Known examples in the II–I_2–IV-Ch_4 system form in one of the seven noncentrosymmetric space groups: $I\bar{4}2m$ (II = Ba, Sr, or Eu, I = Li or Ag, IV = Si, Ge, or Sn, and Ch = S or Se),[20-25] $I222$ ($BaAg_2SnS_4$),[23] $P3_1$ or $P3_2$ enantiomers (II = Ba or Sr, I = Cu, IV = Sn or Ge, and Ch = S),[26-28] $P3_121$ or $P3_221$ enantiomers (II = Ba, Sr, or Eu, I = Cu or Ag, IV = Si, Ge or Sn, and Ch = S or Se),[21,26,29-31] and *Ama*2 (II = Eu, I = Cu, IV = Ge or Sn, and X = S or Se).[29,32,33] Among these, those forming in the $I\bar{4}2m$ space group are related to the chalcopyrite structure type and typically show enhanced SHG activity. Conversely, compounds with the II_3–I_2–IV_2–Ch_8 composition forming in the noncentrosymmetric $I\bar{4}3d$ space group include $Sr_3Ag_2Si_2S_8$,[22] $Sr_3Ag_2Sn_2S_8$,[34] $Sr_3Ag_2Ge_2S_8$,[34] and $Sr_3Ag_2Ge_2Se_8$.[35] While the Ba and Sr chemistry of these systems has been intensely explored, the known Eu(II)-based analogues are much more limited. The few known Eu(II)-based chalcogenides in these systems crystallize in alternate structure types, e.g., Li_2EuGeS_4 or $Cu_2Eu(Ge,Si)Se_4$, and exhibit low or no reported SHG activity.[25,29,32]

Described herein is the synthetic discovery of four Eu(II)-based quaternary chalcogenides with very large mid-IR SHG activities and noncentrosymmetric structures crystallizing in the desired $I\bar{4}2m$ or $I\bar{4}3d$ space groups. These compounds were prepared during high-temperature synthetic investigations in the $EuAg_2IVCh_4$ and $Eu_3Ag_2IV_2Ch_8$ (IV = Sn or Ge; Ch = S or Se) systems and represent the first reported compounds within the Eu–Ag–IV–Ch quaternary systems. Each was synthesized as single crystals for structure determination as well as in bulk powder form. Additional characterization methods included temperature dependent magnetic susceptibility, UV-Vis diffuse reflectance spectroscopy, and SHG activity at the mid-infrared wavelength of 2.09 µm. Their electronic structures were also probed with the use of spin-polarized electronic structure calculations, revealing the impact of the

3

atomic contributions and, especially, the Eu(II) $4f^7$-based states to the band edge states, the bandgap types, band dispersions, as well as the SHG activity.

2. Experimental.

2.1. Reagents Used. Single crystals and bulk polycrystalline powders of **I** to **IV** were synthesized using the following reagents: Eu ingot (Alfa Aesar, 99.9% purity), Ag_2S powder (Alfa Aesar, 99.99% purity), Ag powder (Alfa Aesar, 99.99% purity), Sn ingot (Alfa Aesar, 99.99% purity), S powder (Sigma Aldrich, 99.99% purity), Ge powder (Alfa Aesar, 99.99% purity), and Se powder (Alfa Aesar, 99.99% purity). As Eu metal is air-sensitive, all the chemical manipulations were carried out inside an Argon-filled dry glove box.

2.1.1. *Synthesis of EuAg$_2$GeS$_4$* (**I**). Transparent yellow-colored single crystals of **I** were synthesized from stoichiometric starting materials of Ag_2S powder (43.6 mg, 0.176 mmol), Eu metal chunk (26.7 mg, 0.176 mmol), Ge ingot (12.8 mg, 0.176 mmol), and S powder (16.9 mg, 0.527 mmol), which were loaded into a 6 mm outer diameter (OD) and 4 mm inner diameter (ID) fused silica tube inside the Ar-filled dry glove box. The reaction ampoule was then evacuated to 10^{-4} Torr and sealed with a flame torch. This was then heated to 1123 K in 10 h inside a programmable muffle furnace. The furnace was then annealed for 60 h before slowly cooling to room temperature over 30 h. A pure polycrystalline phase of **I** was synthesized by heating the reactants to 1023 K in 10 h and annealing for 60 h before allowing the furnace to radiatively cool to room temperature. This product was next ground inside the glove box and compressed to an 8 mm diameter circular disk using a hydraulic press. The disk was flame-sealed again inside a ~12 mm OD fused-silica tube. The reaction was annealed for 30 h at 1023 K. The product was then homogeneously ground inside the glove box and the phase purity was analysed using a powder X-ray diffraction. Diffraction peaks were observed corresponding to the formation of a pure polycrystalline phase of **I**.

2.1.2. *Syntheses of Eu$_3$Ag$_2$Ge$_2$Se$_8$* (**II**) *and Eu$_3$Ag$_2$Sn$_2$Se$_8$* (**III**). Transparent block-shaped red-colored single crystals of **II** and **III** were synthesized using identical conditions starting from stoichiometric amounts of Eu metal (31.5 mg, 0.207 mmol), Ag (14.9 mg, 0.138 mmol), Ge (10 mg, 0.138 mmol) and Se (43.6 mg, 0.552 mmol) for **II** and Eu metal (29.6 mg, 0.195 mmol), Ag (14 mg, 0.130 mmol), Sn (15.4 mg,

4

0.130 mmol), and Se (41 mg, 0.519 mmol) for **III**. The elemental starting materials were loaded inside the Ar-filled dry glove box and vacuum sealed under ~10^{-4} Torr pressure. The tubes were heated to 1123 K in 18 h inside a programmable muffle furnace and then slowly cooled to room temperature at a rate of 20 K h^{-1}. The reaction ampoules were opened in air and the products analyzed separately under an optical microscope to reveal the block shaped red-colored crystals for each. Relatively high-purity bulk powders of **II** and **III** were synthesized using a two-step solid-state syntheses method from the respective stoichiometric amounts of the elemental starting materials with a total mass of 400 mg for each. The reagents were loaded into a 12 mm outer diameter (OD) carbon-coated fused silica tube that was flame sealed and slowly heated to 1123 K over 16 h and annealed for 60 h. The resulting ingots were ground inside a Ar-filled glove box and pressed to a circular disk using a hydraulic press. The disks were next annealed for 48 h at 823 K. The resulting products were characterized by powder XRD analyses and found to be pure polycrystalline phases of **II** and **III**.

2.1.3. *Synthesis of $Eu_3Ag_2Sn_2S_8$* (**IV**). Red-colored single crystals of **IV** were synthesized starting from a 100 mg loaded composition using Eu metal (24.7 mg, 0.163 mmol), Ag (35.1 mg, 0.325 mmol), Sn (19.3 mg, 0.163 mmol), and S (20.9 mg, 0.652 mmol). The reactions were prepared and performed similarly to that described above for **I-III**. The reaction was slowly heated to 1023 K over 16 h, annealed for 48 h, and then cooled slowly to 573 K over 20 h. The furnace was next allowed to radiatively cool to room temperature. High-purity bulk powder of **IV** was prepared using a two-step solid-state synthesis method, like that described above for **I** to **III**. Initially, a stoichiometric amount of elemental starting materials of Eu (98.8 mg, 0.652 mmol), Ag (140.4 mg, 1.300 mmol), Sn (77.2 mg, 0.652 mmol), and S (83.6 mg, 2.608 mmol) were massed and loaded into a carbon-coated fused silica tube that was then flame sealed. The reaction was heated to 1023 K over 16 h, annealed at that temperature for 60 h, and then allowed to radiatively cool to room temperature. After pressing the product powder into a circular disk, it was then reheated to 823 K for 48 h. The resulting product was checked by powder XRD analysis to be predominantly polycrystalline **IV** with the co-formation of a minute amount of a secondary phase as shown in Figure S6.

5

2.2. Characterization and Property Measurement Techniques.

2.2.1.   Structure Determination using Single-Crystal XRD. The crystal structures were determined from room temperature (300 K) single crystal X-ray diffraction (SCXRD) datasets of suitable yellow and red block-shaped crystals of $EuAg_2GeS_4$ and $Eu_3Ag_2IV_2Ch_8$ (IV = Ge and Sn and Ch = S and Se) collected using a monochromatized Mo-Kα (λ = 0.71073 Å) radiation source on a Bruker D8 venture diffractometer. Suitable EDS-analyzed crystals of $EuAg_2GeS_4$ (**I**), $Eu_3Ag_2Ge_2Se_8$ (**II**), $Eu_3Ag_2Sn_2Se_8$ (**III**), and $Eu_3Ag_2Sn_2S_8$ (**IV**) were picked separately on a transparent loop under viscous Paratone-N oil and mounted on the goniometer head to collect the intensity data. The crystal qualities were judged from initial fast scan datasets of 180 frames. The APEX4 software[36] was used to determine the unit cell constants for all four different crystals and entire datasets were collected as intensity data. An operating voltage of 50 kV and a working current of 1.4 mA were used for the data collection. An exposure time, frame width, and detector to crystal distance of 3 secs/frame, 0.5º, and 5 cm, respectively were used for the separate data collection of the crystals. The intensity data were integrated using the APEX4 program[36] and the absorption corrections were carried out using the multi-scan method of the SADABS software.[37]

The XPREP program[38] suggested tetragonal or cubic body-centered (I) cells for the crystals of **I**, **II**, **III**, and **IV**. XPREP program indicated the noncentrosymmetric $I\bar{4}2m$ and $I\bar{4}3d$ space groups for the $EuAg_2GeS_4$ and the $Eu_3Ag_2IV_2Ch_8$ crystals, respectively. The crystal structures were solved in respective space groups using the direct method of the SHELXS program of the SHELX-14 suite of programs.[39] The asymmetric unit of the initial solved model of the crystal structure of **I** gave four crystallographically-independent atomic sites, which were then assigned to one Eu, one Ag, one Sn, and one S sites based on coordination environments and peak heights. The initial structural solutions of **II**, **III**, and **IV** crystals gave six crystallographically-independent atomic sites, which were then further assigned to respective atoms based on peak heights and coordination environments. The final solution model provided one Eu, one IV, two Ag, and two Ch sites. Except for the Ag sites, all other atoms are fully occupied. The atomic positions, anisotropic displacement parameters, weight corrections, and extinction parameters were further refined using the least square on the F^2 method of the SHELXL program.[40]

6

The symmetries of the final models were verified using the ADDSYM program of the PLATON software package.[41] The atomic positions were then standardized using the STRUCTURE TIDY program[42] of PLATON. The Wyckoff positions and site symmetries are provided in the Supplementary Information. The crystallographic refinement and metric details are provided in Table 1 and Supporting Information.

Table 1. Structural data and crystallographic refinement details for **I** to **IV**.[a]

Compound	$EuAg_2GeS_4$	$Eu_3Ag_2Sn_2S_8$	$Eu_3Ag_2Sn_2Se_8$	$Eu_3Ag_2Ge_2Se_8$
Space group	$I\bar{4}2m$	$I\bar{4}3d$	$I\bar{4}3d$	$I\bar{4}3d$
a (Å)	6.8305(3)	14.2876(3)	14.8559(5)	14.5943(3)
c (Å)	7.5722(7)			
V (Å^3)	353.29(5)	2916.61(18)	3278.7(3)	3108.49(19)
Z	2	8	8	8
ρ (g. cm^{-3})	5.344	5.288	6.205	6.184
μ (mm^{-1})	19.49	19.75	34.26	36.88
R $(F)^b$	0.025	0.020	0.021	0.027
$R_w(F_o^2)^c$	0.065	0.052	0.050	0.066
S	1.12	1.10	1.10	1.09
No. reflections	3676	15553	11132	10645
No. indep. reflections	301	601	685	656

[a]λ = 0.71073 Å, T = 300(2) K.

[b]$R(F) = \Sigma\ ||F_o|-|F_c||\ /\ \Sigma|F_o|$ for $F_o^2 > 2\sigma(F_o^2)$.

[c]$R_w(F_o^2) = \{\Sigma\ [w(F_o^2 - F_c^2)^2]\ /\ \Sigma wF_o^4\}^{1/2}$. For $F_o^2 < 0$, $w = 1/[\sigma^2(F_o^2) + (mP)^2 + nP]$; where $P = (F_o^2 + 2F_c^2)/3$. Where m and n are 0.0383 and 0.6088 for **I**, 0.0314 and 17.8241 for **IV**, 0.0167 and 38.1439 for **III**, and 0.0363 and 79.4372 for **II**, respectively.

2.2.2. Characterization of Bulk Polycrystalline Powders by Powder XRD and SEM Techniques. All products were ground in air using a mortar and pestle to prepare homogeneous polycrystalline powders. Room temperature powder XRD data were

7

collected for all product samples using Cu-Kα radiation (λ = 1.54 Å) on a PANalytical Empyrean X-ray diffractometer with a working voltage and an operating current of 45 kV and 40 mA. The measured data ranged from from 5º to 75º using a step size increment of 0.013º. Analyses of the approximate chemical compositions of the crystals were probed using energy-dispersive X-ray spectroscopy (EDX) study on a JEOL SEM 6010LA instrument at an accelerating voltage of 20 kV. Representative single crystals and powders were stuck onto a carbon tape adhesive for mounting to a sample pedestal. The elemental EDX data of selected crystals showed only Eu, Ag, IV (Sn or Ge), and Ch (S or Se) atoms in the approximate ratios of 1:2:1:4 and 3:2:2:8 as depicted in the Supporting Information in Figures S1 to S4.

2.2.3. Solid State UV-Vis-NIR Spectroscopy Methods. Room temperature solid-state UV-Vis-NIR spectroscopy data for the polycrystalline samples of **I** to **IV** were recorded in the form of reflectance data as a function of wavelength using a Shimadzu UV3600 instrument. The data were collected from 1000 nm (1.24 eV) to 250 nm (4.96 eV) using dried $BaSO_4$ as a reference. The reflectance data were converted to absorption data using the Kubelka-Munk equation: $\alpha/S = (1 - R)^2/2R$.[43] Here S, α, and R represent the scattering coefficient, absorption coefficient, and reflectance, respectively. The band gaps for the polycrystalline $Eu_3Ag_2IV_2Ch_8$ samples were calculated using the Tauc plot:[43]

$$(\alpha h\gamma)^n = A(h\gamma - E_g)$$

Here A, γ, h, and E_g are the proportionality constant, frequency of light, Planck's constant, and band gap, respectively. The n = ½ and 2 values for the constant indicate the indirect band gap and direct band gap, respectively.

2.2.4. Temperature Dependent Magnetic Susceptibility. The magnetic susceptibility data of all the polycrystalline samples were collected using a Quantum Design MPMS VSM squid instrument using a magnetic field of 10 T over a temperature range of 17 K to 300 K. The polycrystalline samples were loaded separately into Gelatin capsules and the capsules were then loaded inside a straw to collect the magnetic susceptibility data.

2.2.5. Second Harmonic Generation (SHG) Measurements. Room temperature mid-infrared (IR) SHG data were measured using a modified Kurtz-Perry system with a Ho:YAG laser at the wavelength of 2.09 μm.[44] The finely ground polycrystalline

8

powders were sieved to 63–75 µm and measured with $AgGaS_2$ (AGS) as the reference sample. A photomultiplier tube was used to collect the intensity of the frequency-doubled output data emitted from the sieved powdered samples.

2.2.6. Electronic Structure Calculations. Density-functional theory methods were employed with the project augmented wave method as implemented in the Vienna *Ab Initio* Simulation Package (VASP; ver. 6.4.2) for the electronic structure calculations of **I** to **IV**.[45,46] Electron exchange and correlation were treated within the generalized gradient approximation of Perdew-Burke-Ernzerhof (PBE). Calculations were set with an energy convergence criterion of 10^{-8} eV/cell and an energy cutoff of 400 eV for the plane wave basis set, and using the PAW pseudopotentials for Eu ($5s,5p,6s,4f,5d$), Ag ($5s,4d$), Sn ($4d,5s,5p$), Ge ($3d,4s,4p$), Se ($4s,4p$), and S ($3s,4p$) in their respective structures. Their refined structures served as starting models for full geometry relaxation under the respective symmetry constraints until the norms on the atomic forces reached < 0.01 eV $Å^{-1}$. Vacancy disorder for the two Ag sites in the structures of **II**, **III** and **IV** were modelled as described previously for this structure type.[47] Next, spin-polarized densities-of-states (DOS) calculations were performed using an 8 × 8 × 8 k-point mesh (total: 75 k-points) for **I** and 4 × 4 × 4 k-point meshes (total: 36 k-points) for **II** to **IV.** An effective on-site Coulomb interaction for the Eu 4f orbitals was approximated at 6 eV, consistent with prior literature.[48] Next, their spin-polarized band structures were calculated following the standard k-point paths of their respective crystal systems,[49] with either 10 (for **I**) or 15 (for **II** to **IV**) k-point intersections along each Brillouin zone direction. For **I**, this standard path came to a total of 90 k-points along Γ-X-P-N-Γ-M-S|S$_0$-Γ|X-R|Γ-M, while for the structures of **II** to **IV** this consisted of a total of 90 k-points along Γ-H-N-Γ-P-H|P-N|. Individual contributions from the atomic orbitals were projected out as part of each calculation.

3. Results and Discussion

3.1. Synthetic Investigations. Synthetic investigations of the Eu-Ag-IV-Ch (IV = Sn or Ge; Ch = S or Se) system, i.e., with one of four possible combinations of Ge:S, Ge:Sn, Sn:S and Sn:Se, uncovered the first known quaternary chalcogenides combining the Eu(II) and Ag(I) cations. Each could be attained having either the Eu-Ag_2-IV-Ch_4 or Eu_3-Ag_2-IV_2-Ch_8 compositions. The relative closeness of the two

9

compositions led to the preferential formation of one of the two possible structures under these reaction conditions, such as the formation of the former composition only found for $EuAg_2GeS_4$ (**I**). Theoretically, this compound can be converted to the alternate compositions of compounds **II** to **IV** via the reaction: $EuAg_2GeS_4$ + 2 EuS + GeS_2 → $Eu_3Ag_2Ge_2S_8$. However, an incomplete knowledge regarding the thermodynamically competing phases, as well as disorder over the Ag-site in the Eu_3-Ag_2-IV_2-Ch_8 structure (see below), currently prevents a more detailed probing of the relative energetic stabilities of the two compositions with respect to binaries/ternaries.

3.2 Structural Characterization by Single Crystal XRD. High-temperature reactions at 1123 K produced $EuAg_2GeS_4$ (**I**) in the form of block-shaped yellow-colored crystals in a yield of ~75%. A somewhat lower synthesis temperature of 1023 K produced a high purity bulk powder of **I** that was found to be air stable for at least two weeks. The structure of **I**, shown in Figure 1, crystallizes in the noncentrosymmetric $I\bar{4}2m$ tetragonal space group with the unit cell dimension of a = 6.8305(3) Å and c = 7.5722(7) Å. Its structure is comprised of a 3D $[Ag_2GeS_4]^{2-}$ network that is charge-balanced by Eu(II) cations within the cavities. This structure is related to the chalcopyrite-type structure, having a similar body-centered tetragonal cell as shown side-by-side in Figure 1b for $AgGaS_2$.[50] Notably, the structure is a highly compressed version of the $AgGaS_2$ structure type, with the replacement of ½ of the Ag atoms by Ge and replacement of all of the Ga atoms on the faces by Eu and Ag
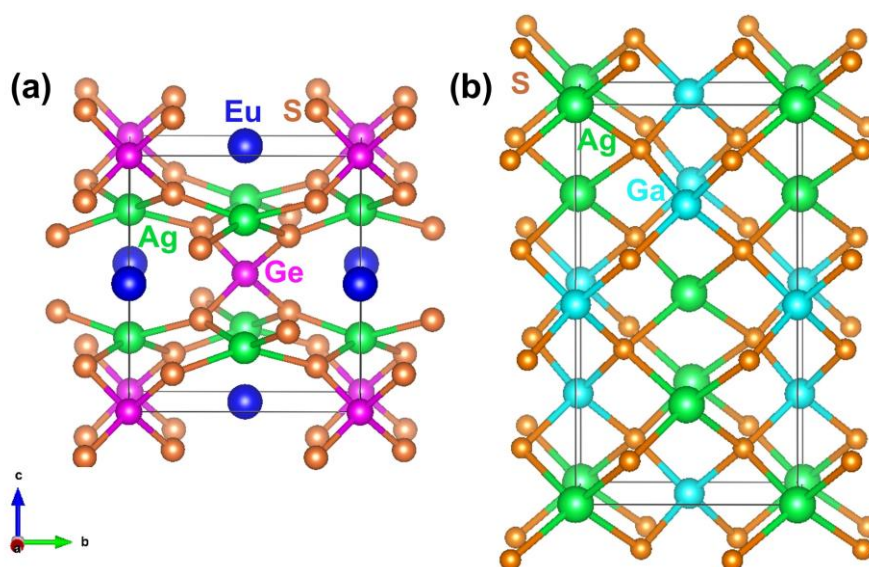
Figure 1. View of the unit cell of (a) $EuAg_2GeS_4$ (space group: $I\bar{4}2m$) and (b) $AgGaS_2$ ($I\bar{4}2d$) crystal structures approximately along the [100] direction.

10

atoms, i.e., $AgGaS_2 \rightarrow (EuAg)(AgGe)S_4$ or written as $EuAg_2GeS_4$. Thus, the crystal structure of **I** can be viewed as a substitutional variant of the parent, noncentrosymmetric, $AgGaS_2$ structure that maintains its breaking of the inversion symmetry. Briefly, the structure of **I** consists of layers of highly flattened AgS_4 tetrahedra, Figure 2a, that are bridged by layers of more regular GeS_4 tetrahedra and Eu(II) cations, Figure 2b. The GeS_4 are all aligned together, Figure S9, and breaking inversion symmetry. Condensation of these layers leads to the formation of a 3D $[Ag_2GeS_4]^{2-}$ network with Eu(II) cations within the cavities.
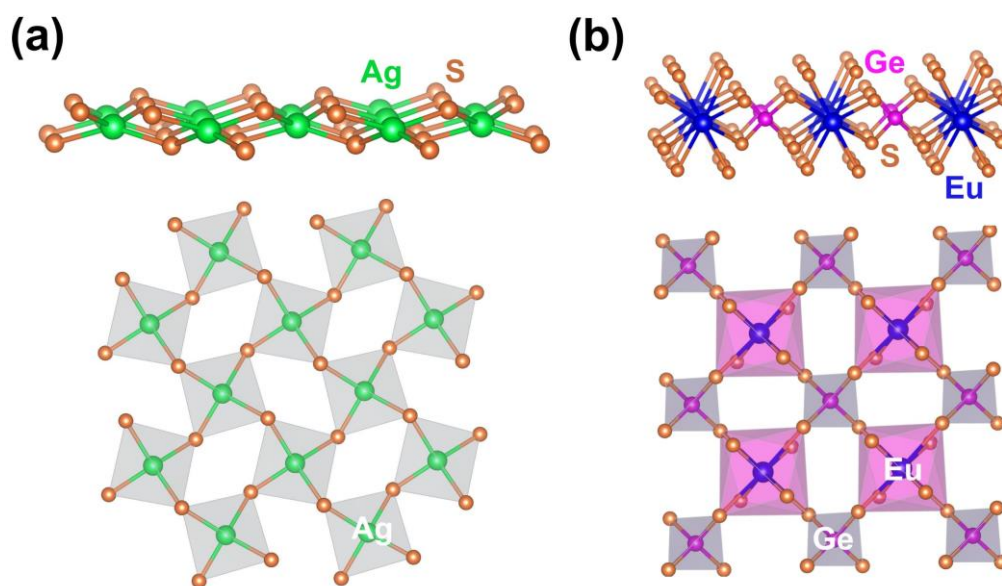
Figure 2. Structural views of the alternating layers of (a) vertex-sharing, flattened AgS_4 tetrahedra and (b) alternating, bridged, GeS_4 tetrahedra and EuS_8 polyhedral units in **I**.

More locally, each of the GeS_4 tetrahedra shares vertices with eight adjacent AgS_4 tetrahedral units. Conversely, each of the AgS_4 flattened tetrahedra shares four vertices with four adjacent AgS_4 tetrahedral units, Figure 2a, as well as shares four vertices with four GeS_4 tetrahedra located above and below the layer. All four Ag–S and Ge–S distances are equivalent by symmetry, as listed in Table S3 for selected near-neighbor distances and angles. The Ag–S distance of 2.5700(6) Å can be compared with the Ag – S distances in isostructural compounds such as $SrAg_2GeS_4$ (2.5744(5) Å),[22] $SrAg_2SiS_4$ (2.5757(4) Å),[22] and $BaAg_2GeS_4$ (2.594(3) Å).[23] Whereas the Ge – S distances of 2.209(2) Å agree well with the Ge–S distances in $SrAg_2GeS_4$ (2.213(2) Å),[22] $BaAg_2GeS_4$ (2.210(4) Å),[23] and $BaCdGeS_4$ (2.200(2)–2.238(1) Å).[51] The Eu –S distances varied from 3.139(2) Å to 3.244(2) Å, which is close to distances

11

found in the previously reported $EuCu_2SnS_4$ (3.0497(8)–3.1444(6) Å),[32] $EuCu_2SiS_4$ (3.1013(8)–3.1655(9) Å),[29] and α-$EuZrS_3$ (3.033(1)–3.290(1) Å).[52]

In contrast, high-temperature reactions for the other three Eu-Ag-IV-Ch combinations (i.e., IV:Ch = Ge:Se, Sn:Se and Sn:S; **II**, **III** and **IV**) each yielded red-colored crystals with the slightly modified composition of $Eu_3Ag_2IV_2Ch_8$. Yields of the $Eu_3Ag_2IV_2Ch_8$ compounds varied from 60% to 80% and showed excellent stability in air for at least two weeks, as characterized by powder XRD. Their structures all crystallized in the cubic, noncentrosymmetric $I\overline{4}3d$ space group with the previously reported $Sr_3Ag_2Ge_2Se_8$ structure type.[34,35] This complex structure, shown in Figure 3 for **III**, can generally be described as the cubic-closest packing of $SnSe_4$ tetrahedra with additional tetrahedra filling all octahedral and tetrahedral sites, i.e., with 16 $SnSe_4$ tetrahedra per unit cell arranged as in the packing of a 'Li$_3$Bi' parent type. As described
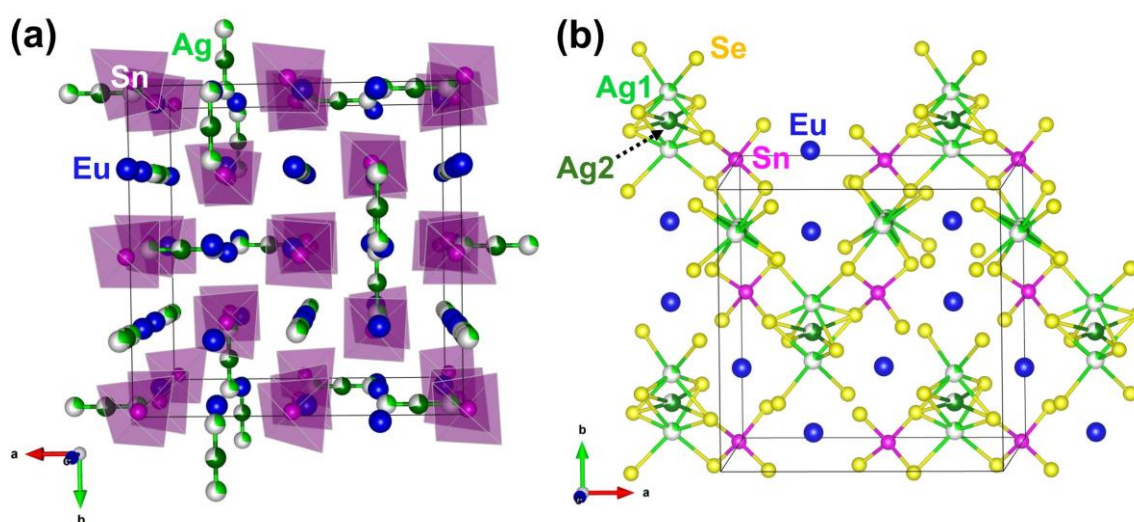
Figure 3. (a) Polyhedral view of the unit cell of **III**, $Eu_3Ag_2Sn_2Se_8$, approximately along the *c*-axis direction with $SnSe_4$ tetrahedra in purple, the split Ag-Ag distances in green, with the Se atoms not shown for clarity, and (b) view of a (110) structural slice showing the local coordination environments of the split Ag(I)/Ag(II) positions and all Ag-Se and Sn-Se bonds < 3.45 Å.

above for **I**, alignment of these tetrahedra break the crystalline inversion symmetry. Listed in Table S5, the Ge–Se, Sn–Se and Sn–S distances of **II**, **III** and **IV** range within comparable distances to those reported in prior studies, such as for $Ba_9Hf_3Sn_2Se_{19}$ (2.503(1)–2.541(1) Å),[15] $Ba_7Sn_3Se_{13}$ (2.477(1) – 2.534(1) Å).[53] $BaCdGeSe_4$ (2.343(1)–2.392(1) Å),[54] $SrCdGeSe_4$ (2.327(2)–2.381(2) Å),[55] $BaCdSnS_4$ 2.353(1)–2.419(1) Å) and $Ba_3CdSn_2S_8$).[56] In contrast to **I**, the structures of **II** to **IV** contain two partially-occupied Ag positions Ag(1) and Ag(2) at the respective Wyckoff sites of 24*d* and 12*a*

12

with different multiplicities. For each structure, the Ag(1) and Ag(2) sites consistently refined (with no constraints) to the respective occupancies of 0.31(1) and 0.71(1) for **II**, 0.28(1) and 0.71(2) for **III**, and 0.31(1) and 0.70(2) for **IV**, and thus the refined compositions of $Eu_3Ag_{1.99(1)}Ge_2Se_8$, $Eu_3Ag_{1.92(1)}Sn_2Se_8$, and $Eu_3Ag_{1.96(1)}Sn_2S_8$. These fall, within reasonable error, close to the nominal compositions for each based on charge-balancing and structural considerations, as described in further detail below.
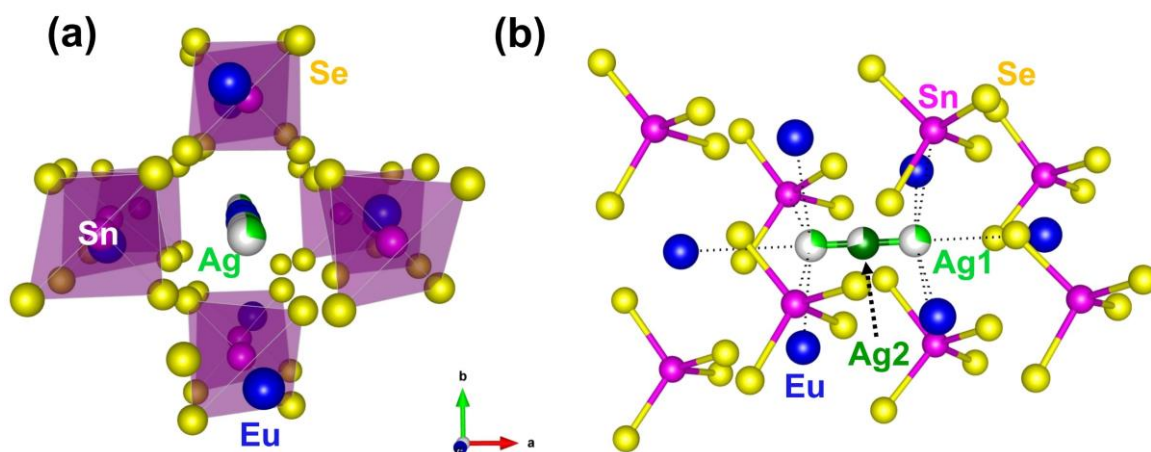

Figure 4. (a) Polyhedral view down a channel formed by neighboring $SnSe_4$ tetrahedra filled with Eu(II) and Ag(I) cations, and (b) Ag1-Ag2-Ag1 'trimer' viewed horizontally with the shorter Ag(1)-Sn (~3.5Å) and Ag(1)-Eu distances (~3.7Å) labelled with dashed lines.

Both the Ag(I) and Eu(II) cations are located within channels that are aligned down each of the symmetry-equivalent [100] / [010] / [100] directions formed by the packing of the $SnSe_4$ tetrahedra, as labelled in Figure 3b and shown for a single channel in Figure 4. The Eu(II) cations coordinate as $EuCh_8$ polyhedra, as in **I**, with respective Eu–Ch distances consistent with those found in $EuHfSe_3$ and other compounds.[57-59] The Ag(2) atom is coordinated in a highly flattened $AgSe_4$ tetrahedral environment with Ag–Se distances of 2.6716(9) Å (×4), and bridges to four neighboring $SnSe_4$ tetrahedra to form its 3D network. Conversely, the split position for the Ag(1) atom is located on opposing sides of each $Ag(2)Se_4$ tetrahedron and is itself coordinated in a distorted octahedral environment, $AgSe_6$, with two short (2.695(7) Å (×2)), and four longer Ag – Se distances (3.319(1) Å (×2); 3.402(1)Å (×2)). A view of the condensation of the $Ag(1)Se_4$ and $Ag(2)Se_6$ polyhedra are shown together in Figure 3(b). The short Ag(1)···Ag(2) distances of ~1.4 to 1.6 Å in **II** to **IV** precludes the simultaneous occupancy of both sites, i.e., with each 'trimeric Ag(1)-Ag(2)-Ag(1) cavity' being occupied either by a central Ag(2) or the opposing Ag(1) positions. Consistent with this, their fractional occupancies sum to a full occupancy, with the

Ag(2) site at ~70% and the Ag(1) site at ~30% occupancy. Occupancy at the Ag(1) site is less energetically favorable, with much shorter distances to three neighboring Eu(II) cations and two Sn(IV) cations, as labelled by dashed lines in Figure 4(b). This raises the question of why the Ag(1) position would be partially occupied? Considering a zero occupancy of the Ag(1) site and a 100% occupancy of only the Ag(2) site, the site multiplicity of 12 for the latter would render the compound electron deficient. Conversely, a fully occupancy of only the Ag(1) site, at a higher multiplicity of 24, would be excess in electrons. Thus, the optimal charge balance of the framework is only attained by the mixed fractional occupancies of both the Ag(1) and Ag(2) sites, as is probed further in the magnetic data and the electronic structure calculations below.

3.3. Magnetic Susceptibilities. As a probe of the oxidation states of the Eu(II) in compounds **I** to **IV**, their temperature-dependent magnetic responses were measured as a function of temperature. The magnetic susceptibilities (χ) and inverse magnetic susceptibilities ($1/\chi$) versus were plotted versus temperature in Figure 5. Each follows a paramagnetic behaviour that could be fitted to the standard Curie-Weiss equation:
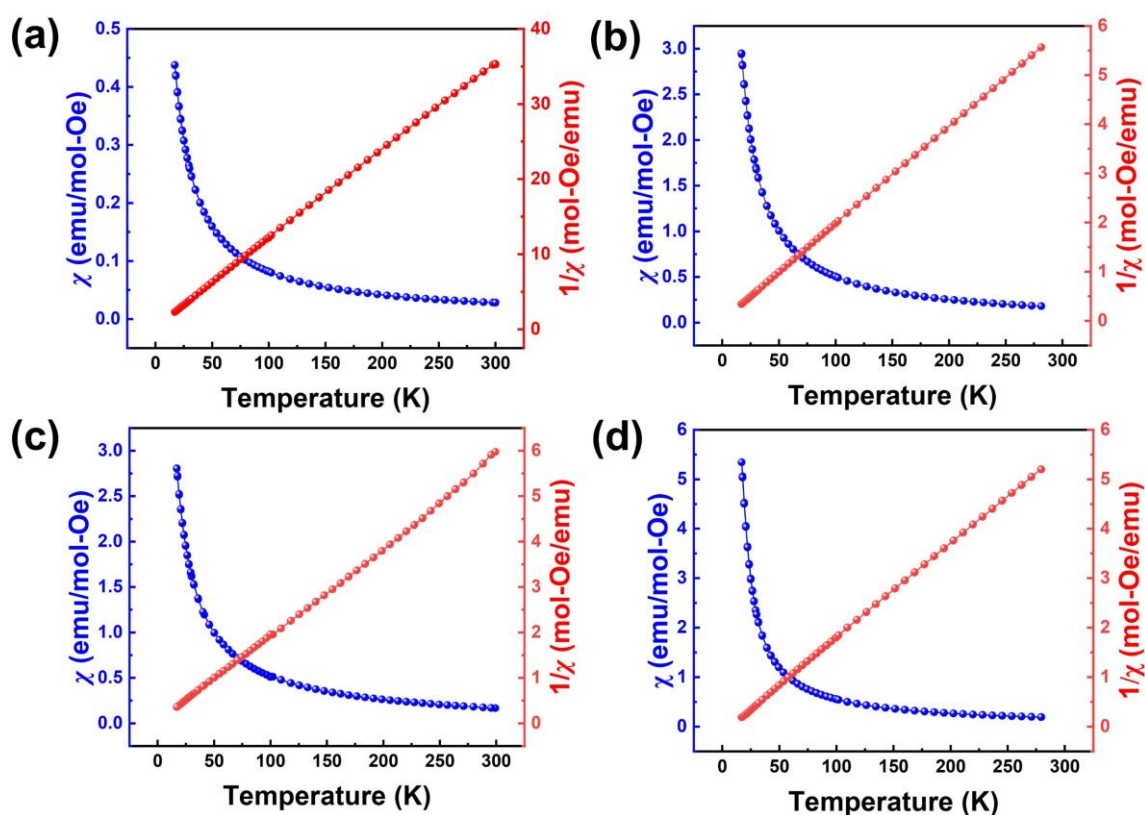

Figure 5. Plots of magnetic susceptibilities (χ; blue) and inverse magnetic susceptibilities ($1/\chi$; red) versus temperature (K) for bulk crystalline powders of (a) **I** (EuAg$_2$GeS$_4$), (b) **II** (Eu$_3$Ag$_2$Ge$_2$Se$_8$), (c) **III** (Eu$_3$Ag$_2$Sn$_2$Se$_8$), and (d) **IV** (Eu$_3$Ag$_2$Sn$_2$S$_8$).

14

$\chi(T) = C/(T-\theta)$. Here C and θ denote the Curie constants and Weiss constants respectively. The plots of $1/\chi$ versus temperature were fairly linear over the entire temperature range and were fitted well within the temperature interval of 25 to 250 K. These fittings gave Curie-Weiss temperatures of -3.34 K, -0.35 K, -2.38 K. and 5.25 K for **I**, **II**, **III** and **IV**, respectively. These suggest weak predominant antiferromagnetic (**I** to **III**) and ferromagnetic (**IV**) interactions between the Eu cations, which are the only magnetic centers in all four compounds.

The Eu cations is most commonly in either the +2 ($4f^7$) and/or +3 ($4f^6$) oxidation states within metal chalcogenide compounds. The spin-only magnetic moments [μ_{cal} = $\{n(n+2)\}^{1/2}$] for the Eu(II) and Eu(III) cations theoretically are expected to be close to 7.99 μ_B and 6.99 μ_B, respectively. The fitted, experimental, magnetic moments per Eu atom were found to be 8.23 μ_B, 8.21 μ_B, 8.38 μ_B, and 8.36 μ_B, for **I**, **II**, **III** and **IV**, respectively, which is somewhat larger than the spin only magnetic moment value (7.99 μ_B) for the Eu(II) cation. These slightly enhanced magnetic moments are comparable to many isoelectronic, e.g., Eu(II) versus Gd(III), gadolinium intermetallic compounds. From gadolinium magnetochemistry it is well known that an increased moment can be ascribed to the gadolinium $5d$ electrons that induce $4f$–$5d$ exchange interactions.[60,61] Compounds with divalent europium cations are also known to show similar enhanced magnetic moments.[62] Thus, these magnetic moments are most consistent with a Eu(II) oxidation state and with the divalent nature of the II-site cations in this structure type, as is known for Sr(II) and Pb(II) analogues in the reported $Pb_3Ag_2Si_2S_8$ and $Sr_3Ag_2Sn_2S_8$.[35] The oxidation states of the Eu(II) cations are also further confirmed by the assigned oxidation states of Ag(I), Sn(IV)/Ge(IV) in the chemical compositions, as $(Eu^{2+})_3(Ag^{1+})_2(IV^{4+})_2(Ch^{2-})_8$ for **II** to **IV**.

3.4. Optical Properties and Electronic Structures.

3.4.1. Optical Band Gaps. Complex metal chalcogenides have represented attractive semiconductor candidates for optoelectronic-type applications owing to the versatility and tunability of their structures and properties. Within these and related structural families, this includes small visible-light bandgaps, large optical absorption coefficients, high band dispersion as well as functional defect tolerance. The optical bandgaps of **I** to **IV** were assessed using UV-Vis diffuse reflectance spectroscopy on

15
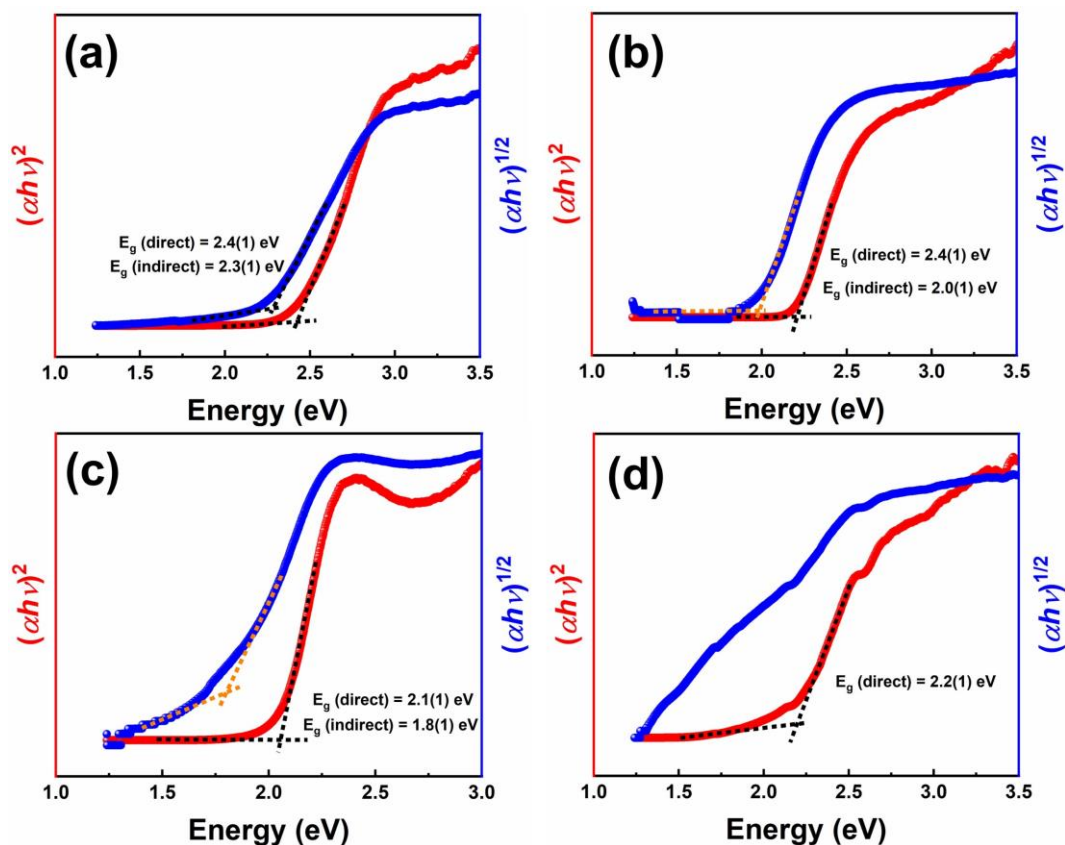
Figure 6. The Tauc plots for the polycrystalline powders of (a) **I** (EuAg$_2$GeS$_4$), (b) **II** (Eu$_3$Ag$_2$Ge$_2$Se$_8$), (c) **III** (Eu$_3$Ag$_2$Sn$_2$Se$_8$), and (d) **IV** (Eu$_3$Ag$_2$Sn$_2$S$_8$).

their polycrystalline powders at room temperature (300(2) K). Their respective Tauc plots were plotted as shown in Figure 6(a-d). The direct band transitions (red curves) for EuAg$_2$GeS$_4$, Eu$_3$Ag$_2$Ge$_2$Se$_8$, Eu$_3$Ag$_2$Sn$_2$Se$_8$, and Eu$_3$Ag$_2$Sn$_2$S$_8$ samples were estimated to be ~2.4 eV for **I** and **II**, ~2.1 eV for **III**, and ~2.2 eV for **IV**, consistent with the colors of their polycrystalline powders. Both **I** and **II** showed evidence for lower energy indirect bandgaps (blue curves) of ~2.3 eV and ~2.0 eV, respectively. The bandgap of **II** is wider than that previously reported for its Sr-based analogue, Sr$_3$Ag$_2$Ge$_2$Se$_8$, at ~1.90 eV. Compound. By contrast, both Sn(IV)-containing compounds exhibited onsets of indirect transitions that were relatively ambiguous, extending to ~1.5 eV and below. Prior studies in the II$_3$–I$_2$–IV$_2$–Ch$_8$ chemical family show that related compounds typically exhibit indirect bandgaps that are lower in energy by only ~0.1 eV or less than kT ("quasi-direct") than the direct transitions,[47] and which would also be consistent with the results of electronic structure calculations for **II** to **IV** (described below). Taken together, this suggests their indirect transitions have likely been obscured by impurities and/or a high degree of structural disorder in the Sn(IV)-containing chalcogenides. Also generally, the Eu(II)-containing compounds

16

exhibit somewhat smaller bandgaps than their Sr-based versions. For example, the quasi-direct bandgap of the Sr-analogue to **IV**, i.e., $Sr_3Ag_2Sn_2S_8$, is reported to be higher in energy at ~2.66 eV.[47]

3.4.2. Second Harmonic Generation (SHG) Activities. Complex metal chalcogenides with chalcopyrite and related structure types with tetrahedral network motifs have also been demonstrated to have among the largest SHG responses and laser induced damage threshold (LIDT) for infrared nonlinear optical applications. Prior research has shown that effective strategies to enhance these properties have included a) the incorporation of rare-earth elements, such as in the cases of $Eu_2P_2S_6$ and Dy_3GaS_6 which have 3.4x and 14x the LIDT at 1.064 µm,[17,18] and b) targeted co-substitutions of alkali or alkaline earth metals with main-group metal cations such as Sn(IV) and Ge(IV) to increase the bandgap and inhibit multi-photon absorptions, such as known in Na_2BaSnS_4 (E_g = 3.27 eV) versus $AgGaS_2$ (2.56 eV in AGS).[19,20]
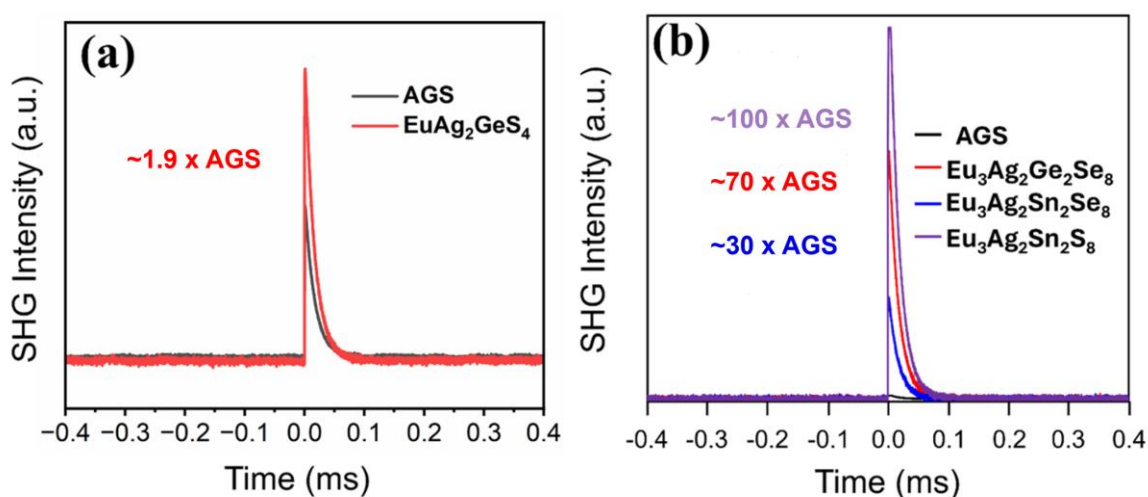
Figure 7. SHG responses versus AGS (black lines) for bulk powders of (a) $EuAg_2GeS_4$ (**I**), and (b) $Eu_3Ag_2Ge_2Se_8$ (**II**), $Eu_3Ag_2Sn_2Se_8$ (**III**), and $Eu_3Ag_2Sn_2S_8$ (**IV**).

The four quaternary chalcogenides, $EuAg_2GeS_4$ (**I**), $Eu_3Ag_2Ge_2Se_8$, (**II**) $Eu_3Ag_2Sn_2Se_8$ (**III**), and $Eu_3Ag_2Sn_2S_8$ (**IV**), represent a potentially effective combination of these strategies. Using a modified Kurtz-Perry method,[44] their SHG activities as powders exhibited remarkably high responses of ~1.9, ~70, ~30, and ~100 (x AGS) at 2.09 µm, shown plotted in Figure 7. Their LIDT was not measured directly. However, the LIDT of each compound is significantly larger than AGS as evidenced by the lack of signal decay and sample destruction over the duration of the measurement. By comparison to other metal chalcogenides with a single anion, as listed in Table 2, these currently represent some of the largest known responses.

17

Table 2. Selected list of currently known metal chalcogenides (single anion) exhibiting high SHG activity.

| Compound	Space Group	E_g (eV)	SHG[a]	Reference
$AgGaS_2$	$I\bar{4}2d$	2.54-2.73	1.00	63
Dy_3GaS_6	$Cmc2_1$	2.81	0.2 × KTP @1.91 μm	18
Na_2BaSnS_4	$I\bar{4}2d$	3.27	0.5	19
$Li_2Ba_7Sn_4S_{16}$	$I\bar{4}3d$	2.30	0.5	63
$Li_2Ba_6MnSn_4S_{16}$	$I\bar{4}3d$	2.76	5.1	64
$SrAg_2GeS_4$	$I\bar{4}2m$	1.73	~0.62 × AGS 1.8 μm	22
$SrAg_2SiS_4$	$I\bar{4}2m$	2.08	~0.59 × AGS 1.8 μm	22
$EuCu_2GeS_4$	$P3_221$	2.32	Not active	29
$EuCu_2SiS_4$	$P3_221$	2.36	Not active	29
$BaLi_2GeS_4$	$I\bar{4}2m$	3.66	~0.5	20
$BaLi_2SnS_4$	$I\bar{4}2m$	3.07	~0.7	20
$EuAg_2GeS_4$	$I\bar{4}2m$	2.4	~1.9 × AGS @2.1 μm	This work
$Eu_3Ag_2Ge_2Se_8$	$I\bar{4}3d$	2.0	~70 × AGS @2.1 μm	This work
$Eu_3Ag_2Sn_2Se_8$	$I\bar{4}3d$	<2.0	~30 × AGS @2.1 μm	This work
$Eu_3Ag_2Sn_2S_8$	$I\bar{4}3d$	<2.0	~100 × AGS @2.1	This work

[a] SHG values are listed in units of x AGS (d_{ij} = 11 pm/V) and @2.09 μm unless otherwise stated.

Amongst an even wider range of noncentrosymmetric materials that contain multiple anions, only a handful have elicited SHG responses this large at this wavelength, such as $Ba_3CsGa_5Se_{10}Cl_2$ and $Ba_3ZnGa_5Se_{10}Cl_2$ (100 and 59 x AGS, respectively),[65,66] or $K_2P_2Se_6$ (~150 x AGS).[67] Interestingly, there is also a small family of compounds with a similar structure to compounds **II** to **IV**, $A_2Ba_7Sn_4Ch_{16}$ (A = Na, Li, Ch = S, Se).[63] These compounds contain similar networks of $SnCh_4$ tetrahedra connected via $(A/Ba)Ch_4$ tetrahedra and Ba atoms within the tunnels. Despite the similar structures and optical band gaps of $A_2Ba_7Sn_4Ch_{16}$ to compounds **II** to **IV**, the SHG responses are orders of magnitude lower (0.1-0.5 × AGS). While **II**, **III** and **IV** exhibit record-breaking SHG responses, currently there are yet few structural and compositional conclusions that can be immediately drawn. The mid-infrared SHG response of the $EuAg_2GeS_4$ sample, Figure 7(a), was found to be ~1.9 × AGS @ 2090 nm and can be compared to the previously reported compounds listed in Table 2. As the $EuAg_2GeS_4$ structure is related to the commercially available NLO material $AgGaS_2$ (chalcopyrite) and the band gap of 2.4(1) eV is very close to the band gap of AGS (2.62 eV), the NLO properties of $EuAg_2GeS_4$ are very promising. Compounds **I-**

18

IV are thus unique compounds and interesting for further investigation into the microscopic origins of their optical properties to better understand their large SHG coefficients, as analyzed below using electronic structure calculations.

3.4.3. Electronic Structure Calculations. The electronic structures of metal chalcogenides have been explored in prior studies for more deeply understanding their optoelectronic properties, such as their bandgap edges and distance, conduction band (CB) and valence band (VB) dispersion and the effective masses of electrons (m_e) and holes (m_h), and tolerance to structural defects. Thus, **I** and the isostructural series of **II** to **IV** represent a key series for examining the microscopic origins of their optoelectronic properties, including an initial assessment of potential relationships with their SHG activities. Electronic structures of several compounds that fall within the II-I_2-IV-Ch_4 and II_3-I_2-IV_2-Ch_8 (Ch = S or Se) chemical families have been reported,[22,47] such as the electronic structure of **I**.[33]

Density functional theory calculations were performed on the fully geometry-relaxed structures of compounds **I** to **IV**, including their spin-polarized density-of-states (DOS) and band structures with the individual atomic orbital contributions projected out. The results for the isostructural series of **II** to **IV** are plotted together in Figure 8,
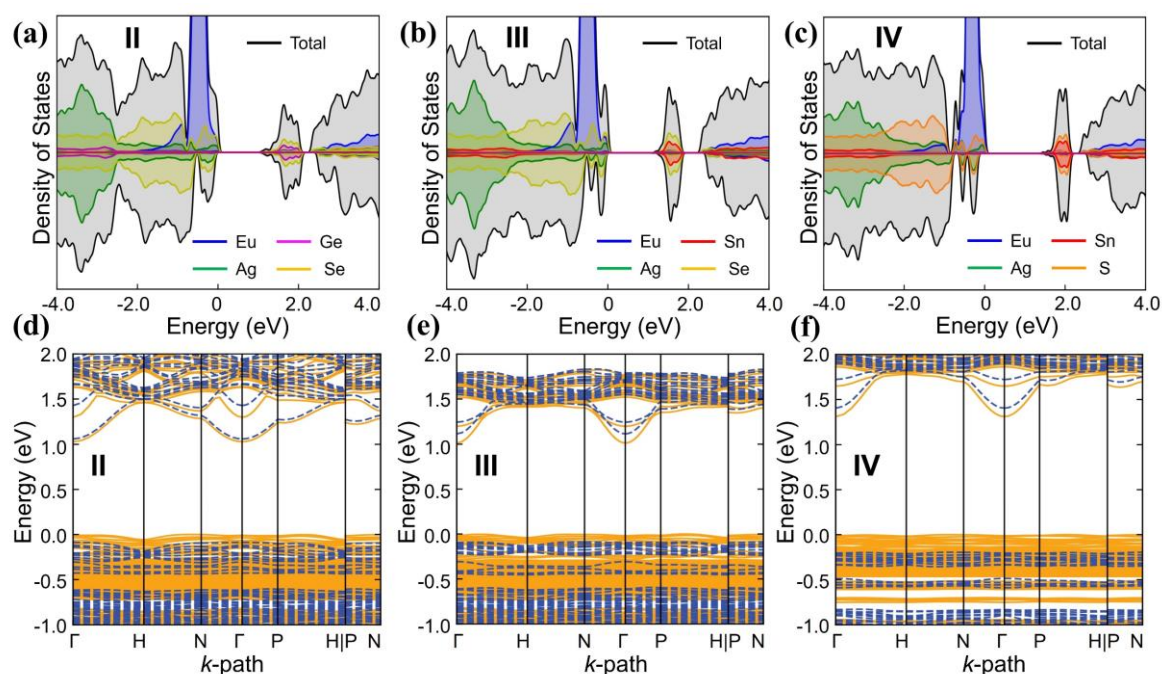
Figure 8. Calculated spin-polarized density of states (DOS; upper) and band structures (lower) for $Eu_3Ag_2Ge_2Se_8$ (**II**; a, d), $Eu_3Ag_2Sn_2Se_8$ (**III**; b, e) , and $Eu_3Ag_2Sn_2S_8$ (**IV**; c, f), with the Fermi level at 0 eV, the atomic orbital contributions labelled with colored lines, and the spin-polarized bands labeled as up (yellow, solid) and down (blue, dashed).

19

while the results for **I** are provided in Figure 9. To begin with the isostructural series, the VB and CB edges of each originate from the filled, Ag($4d$)-S/Se($3p/4p$) states and empty Ge/Sn($4p/5p$)-S/Se($3p/4p$) based states, respectively. In **III**, for example, these contributions correspond to the Ag-/S-based and Sn-/Se-based states at the VB and CB edges. However, in each case, the half-filled Eu(II) $4f^7$ states also significantly contribute a highly-localized band (blue line) near the valence band edges. The Eu-based states shift closer to the VB edge in the order of **III** < **II** < **IV** with a corresponding decrease in the VB dispersion in that order, illustrated in Figure 8. Upon reaching compound **IV**, for example, the Eu $4f^7$ states correspond to the predominant contributions at the VB edge, with the Ag- and S-based states constituting the minor contributions. Iso-surface plots of the electron density near (~0.5 to 0.3 eV) the VB edges are illustrated in Figures S12 to S14 in the Supporting Information. Across this same series of increasing Eu-contributions, i.e., from **III** to **II** to **IV**, the calculated effective hole masses are -2.8, -3.2, and -5.8 m_e. Notably, this trend with increasing Eu $4f^7$ contributions at the VB edge is positively correlated with the SHG activity from ~30 to ~70 to ~100 × AGS for **III** to **II** to **IV**. This is consistent with prior theoretical studies that show higher SHG activity arising from flatter bands as well as from contributions from more polarizable cations at the band edges.[68] Further, calculations predict 'quasi-direct' bandgaps for each, with the indirect bandgaps only minimally smaller (~0.01 to 0.02 eV) than the higher-energy direct band transitions.

Similarly for **I** (EuAg$_2$GeS$_4$), its electronic structure shows VB and CB edges stemming respectively from filled Ag($4d$)-S($3p$) states and empty Ge($4p$)-S($3p$), plotted
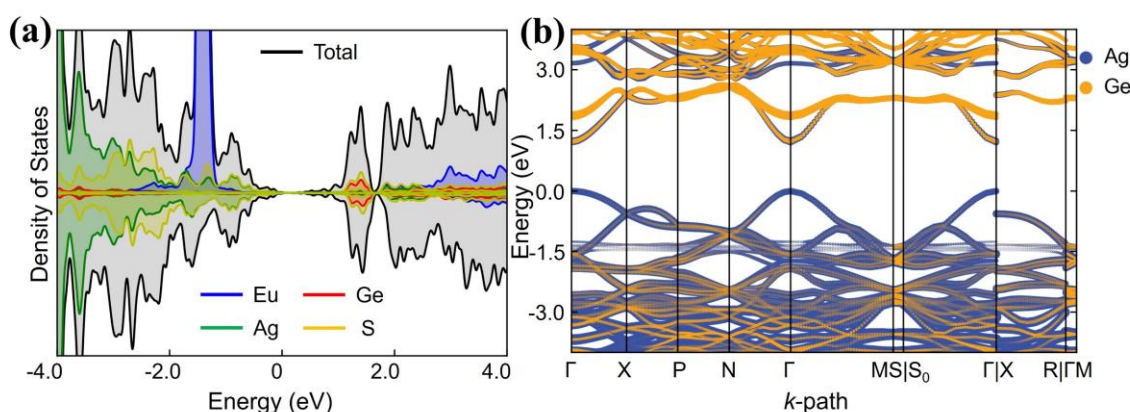
Figure 9. Calculated spin-polarized density of states (DOS; upper) and band structures (lower) for EuAg$_2$GeS$_4$ (**I**) with the Fermi level at 0 eV, the atomic orbital contributions labelled with colored lines, and the spin-polarized bands labeled as up (yellow, solid) and down (blue, dashed).

20

in Figure 9. The electron density of the VB edge is clearly two-dimensional in nature with the greatest degree of band dispersion along the flattened AgS_4-type layers. The CB states show a similarly high band dispersion across the GeS_4 tetrahedra but also showing a small admixture from the Ag($4d$) states throughout the network, most especially near the lowest CB edges seen in the band structure. Consistent with prior reports in the II-I_2-IV-Ch_4 family, the effective masses of carriers at both the CB and VB edges are relatively small at 0.22 m_e and -0.38 m_h, respectively. Further, the Eu $4f^7$-based states are buried much more deeply within the valence band, at ~1.5 eV below the Fermi level, as compared to compounds **II** to **IV**. Its SHG activity is the smallest among the entire series, at only ~1.9 × AGS, and is consistent with the trend as described above. This result also likely helps to explain the absence of significant SHG-activity in the prior Eu(II)-based chalcogenides forming in this structure type, e.g., as reported for Li_2EuGeS_4 and $Cu_2EuSnSe_4$. Further experimental and theoretical research is needed and is ongoing to more deeply understand this relationship between SHG and the electronic structures of Eu(II)-based chalcogenides.

4. Conclusions.

In conclusion, synthetic investigations of the Eu-Ag-IV-Ch (IV = Sn or Ge; Ch = S or Se) systems have unveiled four new Eu(II)-based quaternary chalcogenides that are noncentrosymmetric and exhibit among the largest known mid-IR SHG activities. The four new compounds, $EuAg_2GeS_4$ (**I**), $Eu_3Ag_2Ge_2Se_8$ (**II**) $Eu_3Ag_2Sn_2Se_8$ (**III**) and $Eu_3Ag_2Sn_2S_8$ (**IV**), all consist of body-centered arrangements of oriented (Ge/Sn)Ch_4 tetrahedra that break inversion symmetry. These tetrahedra are bridged together by highly flattened $AgCh_4$ tetrahedra into 3D networks, i.e., $[Ag_2GeS_4]^{2-}$ or $[Ag_2IV_2Ch_8]^{6-}$, and charge balanced by the Eu(II) cations. Measured optical bandgaps occurred over visible-light energies and ranged from ~2.3 eV for the yellow crystals of **I** and ~2.0 to 1.8 eV for the red crystals of **II, III**, and **IV**. Spin-polarized band structure calculations found that their valence band (VB) and conduction band (CB) edge states stem from interactions of the filled Ag-to-S/Se and empty Ge/Sn-to-S/Se based states, respectively. However, a most notable and key shift of the Eu(II) $4f^7$-based to the valence band edge occurred in the order of **I** < **III** < **II** < **IV** and positively correlated with the increasing SHG activity, which ranged from a large ~1.9 × AGS (AgGaS$_2$) for

21

I, to remarkably high values of ~30 for **III**, ~70 for **II**, and ~100 (× AGS) for **IV**. Thus, these results represent some of the highest attained SHG properties within new Eu(II)-based chalcogenides that, in turn, informs new design strategies for the future discovery of advanced, functional NLO materials.

5. Supporting Information.

The crystallographic data files of $EuAg_2GeS_4$, $Eu_3Ag_2Ge_2Se_8$, $Eu_3Ag_2Sn_2Se_8$, and $Eu_3Ag_2Sn_2S_8$ structures are submitted to Cambridge Crystallographic Data Centre (CCDC) with the CCDC numbers of 2356431, 2342594, 2342593, and 2342595, respectively, and can be accessed from CCDC (https://www.ccdc.cam.ac.uk/) at no charge. The SEM data of the elemental composition and mapping, PXRD data, the atomic displacement parameters, and the metric details of the final refined structure are provided in the Supporting Information.

6. Acknowledgements.

7. References.

(1)   Garmire, E. Nonlinear Optics in Daily Life. *Opt. Express, OE* **2013**, *21* (25), 30532–30544.

(2)   Luo, X.; Li, Z.; Guo, Y.; Yao, J.; Wu, Y. Recent Progress on New Infrared Nonlinear Optical Materials with Application Prospect. *J. Solid State Chem.* **2019**, *270*, 674–687.

22

(3)   Pushkarsky, M. B.; Webber, M. E.; Macdonald, T.; Patel, C. K. N. High-Sensitivity, High-Selectivity Detection of Chemical Warfare Agents. *Appl. Physics Lett.* **2006**, *88* (4), 044103.

(4)   Tholl, H. D. Review and Prospects of Optical Countermeasure Technologies. In *Technologies for Optical Countermeasures XV*; SPIE, 2018; Vol. 10797, p 1079702.

(5)   Schunemann, P. G.; Schepler, K. L.; Budni, P. A. Nonlinear Frequency Conversion Performance of $AgGaSe_2$, $ZnGeP_2$, and $CdGeAs_2$. *MRS Bull.* **1998**, *23* (7), 45–49.

(6)   He, J.; Iyer, A. K.; Waters, M. J.; Sarkar, S.; Zu, R.; Rondinelli, J. M.; Kanatzidis, M. G.; Gopalan, V. Giant Non-Resonant Infrared Second Order Nonlinearity in γ - $NaAsSe_2$. *Adv. Opt. Mater.* **2022**, *10* (2), 2101729.

(7)   Bera, T. K.; Jang, J. I.; Song, J.-H.; Malliakas, C. D.; Freeman, A. J.; Ketterson, J. B.; Kanatzidis, M. G. Soluble Semiconductors $AAsSe_2$ (A = Li, Na) with a Direct-Band-Gap and Strong Second Harmonic Generation: A Combined Experimental and Theoretical Study. *J. Am. Chem. Soc.* **2010**, *132* (10), 3484–3495.

(8)   Chung, I.; Kanatzidis, M. G. Metal Chalcogenides: A Rich Source of Nonlinear Optical Materials. *Chem. Mater.* **2014**, *26* (1), 849–869.

(9)   Wu, H.; Yu, H.; Yang, Z.; Hou, X.; Su, X.; Pan, S.; Poeppelmeier, K. R.; Rondinelli, J. M. Designing a Deep-Ultraviolet Nonlinear Optical Material with a Large Second Harmonic Generation Response. *J. Am. Chem. Soc.* **2013**, *135* (11), 4215–4218.

(10)   Tran, T. T.; Yu, H.; Rondinelli, J. M.; Poeppelmeier, K. R.; Halasyamani, P. S. Deep Ultraviolet Nonlinear Optical Materials. *Chem. Mater.* **2016**, *28* (15), 5238–5258.

(11)   Liao, J.-H.; Marking, G. M.; Hsu, K. F.; Matsushita, Y.; Ewbank, M. D.; Borwick, R.; Cunningham, P.; Rosker, M. J.; Kanatzidis, M. G. α- and β-$A2Hg_3M_2S_8$ (A = K, Rb; M = Ge, Sn): Polar Quaternary Chalcogenides with Strong Nonlinear Optical Response. *J. Am. Chem. Soc.* **2003**, *125*, 9484–9493.

(12)   Sun, M.; Xing, W.; Chen, S. K.; Li, C.; Liu, W.; Lee, M.-H.; Yao, J. $ACd_4Ga_5Te_{12}$ (A = K, Rb, Cs): Tellurides with a Strong Nonlinear Optical Response and Purple Emission. *Chem. Mater.* **2023**, *35*, 7218–7228.

(13)   Iyer, A. K.; Cho, J. B.; Waters, M. J.; Cho, J. S.; Oxley, B. M.; Rondinelli, J. M.; Jang, J. I.; Kanatzidis, M. G. Ba_2MAsQ_5 (Q = S and Se) Family of Polar Structures with Large Second Harmonic Generation and Phase Matchability. *Chem. Mater.* **2022**, *34*, 5283–5293.

(14)   Greaney, M. A.; Ramanujachary, K. V.; Teweldemedhin, Z.; Greenblatt, M. Studies on the Linear Chain Antiferromagnets: Ba_2MnX_3 (X = S, Se, Te) and Their Solid Solutions. *J. Solid State Chem.* **1993**, *107*, 554–562.

(15)   Jana, S.; Gabilondo, A.; McGuigan, S.; Maggard, P.A. Syntheses, Crystal Structures, and Electronic Structures of New Quaternary Group-IV Selenide Semiconductors. *Inorg. Chem.* **2024**, *63*, 6474-6482.

(16)   Zhao, L.-D.; Lo, S.-H.; Zhang, Y.; Sun, H.; Tan, G.; Uher, C.; Wolverton, C.; Dravid, V. P.; Kanatzidis, M. G. Ultralow Thermal Conductivity and High Thermoelectric Figure of Merit in SnSe Crystals. *Nature* **2014**, *508*, 373–377.

(17)   Guo, S.-P.; Chi, Y.; Guo, G.-C. Recent Achievements on Middle and Far-Infrared Second-Order Nonlinear Optical Materials. *Coord. Chem. Rev.* **2017**, *335*, 44–57.

(18)   Zhang, M.-J.; Li, B.-X.; Liu, B.-W.; Fan, Y.-H.; Li, X.-G.; Zeng, H.-Y.; Guo, G.-C. Ln_3GaS_6 (Ln = Dy, Y): New Infrared Nonlinear Optical Materials with High Laser Induced Damage Thresholds. *Dalton Trans.* **2013**, *42*, 14223–14229.

(19)   Wu, K.; Yang, Z.; Pan, S. Na_2BaMQ_4 (M=Ge, Sn; Q=S, Se): Infrared Nonlinear Optical Materials with Excellent Performances and That Undergo Structural Transformations. *Angew. Chem. Int. Ed.* **2016**, *55*, 6713–6715.

(20)   Wu, K.; Zhang, B.; Yang, Z.; Pan, S. New Compressed Chalcopyrite-like $Li_2BaM^{IV}Q_4$ (M^{IV} = Ge, Sn; Q = S, Se): Promising Infrared Nonlinear Optical Materials. *J. Am. Chem. Soc.* **2017**, *139*, 14885–14888.

(21)   Yang, Y.; Wu, K.; Wu, X.; Zhang, B.; Gao, L. A new family of quaternary thiosilicates SrA_2SiS_4 (A = Li, Na, Cu) as promising infrared nonlinear optical crystals. *J. Mater. Chem. C* **2020**, *8*, 1762–1767.

(22)   McKeown Wessler, G. C.; Wang, T.; Sun, J.-P.; Liao, Y.; Fischer, M. C.; Blum, V.; Mitzi, D. B. Structural, Optical, and Electronic Properties of Two Quaternary

24

Chalcogenide Semiconductors: Ag_2SrSiS_4 and Ag_2SrGeS_4. *Inorg. Chem.* **2021**, *60*, 12206–12217.

(23)   Chen, H.; Liu, P.-F.; Li, B.-X.; Lin, H.; Wu, L.-M.; Wu, X.-T. Experimental and theoretical studies on the NLO properties of two quaternary non-centrosymmetric chalcogenides: $BaAg_2GeS_4$ and $BaAg_2SnS_4$. *Dalton Trans.* **2018**, *47*, 429–437.

(24)   Nian, L.; Wu, K.; He, G.; Yang, Z.; Pan, S. Effect of Element Substitution on Structural Transformation and Optical Performances in $I_2BaM^{IV}Q_4$ (I = Li, Na, Cu, and Ag; MIV = Si, Ge, and Sn; Q = S and Se). *Inorg. Chem.* **2018**, *57* (6), 3434–3442.

(25)   Aitken, J. A.; Larson, P.; Mahanti, S. D.; Kanatzidis, M. G. Li_2PbGeS_4 and Li_2EuGeS_4: Polar Chalcopyrites with a Severe Tetragonal Compression. *Chem. Mater.* **2001**, *13*, 4714–4721.

(26)   Nian, L.; Huang, J.; Wu, K.; Su, Z.; Yang, Z.; Pan, S. $BaCu_2M^{IV}Q_4$ (M^{IV} = Si, Ge, and Sn; Q = S, Se): Synthesis, Crystal Structures, Optical Performances and Theoretical Calculations. *RSC Adv.* **2017**, *7*, 29378–29385.

(27)   Teske, Chr. L. Darstellung und Kristallstruktur von Cu_2SrSnS_4. *Z. Anorg. Allg. Chem.* **1976**, *419*, 67–76.

(28)   Teske, C. L. Über Die Darstellung Und Röntgenographische Untersuchung von Cu_2SrGeS_4 Und Cu_2BaGeS_4. *Z. Naturforsch. B* **1979**, *34*, 386–389.

(29)   Sun, Z.-D.; Chi, Y.; Guo, S.-P. Cu_2EuMQ_4 (M = Si, Ge; Q = S, Se): Syntheses, Structure Study and Physical Properties Determination. *J. Solid State Chem.* **2019**, *269*, 225–232.

(30)   Sarkar, A.; Viswanathan, G.; Wu, K.; Miller, G. J.; Kovnir, K. $BaCu_2SiS_4$: A New Member of the $A^{II}B^I_2M^{IV}Q_4$ Chalcogenide Family with a Chiral Crystal Structure. *Z. Anorg. Allg. Chem.* **2023**, *649*, e202300147.

(31)   Yang, Y.; Wu, K.; Zhang, B.; Wu, X.; Lee, M.-H. Infrared Nonlinear Optical Polymorphs α- and β-$SrCu_2SnS_4$ Exhibiting Large Second Harmonic Generation Responses with Requisite Phase-Matching Behavior. *Chem. Mater.* **2020**, *32*, 1281–1287.

(32)   Aitken, J. A.; Lekse, J. W.; Yao, J.-L.; Quinones, R. Synthesis, Structure and Physicochemical Characterization of a Noncentrosymmetric, Quaternary Thiostannate: $EuCu_2SnS_4$. *J. Solid State Chem.* **2009**, *182*, 141–146.

(33)   Wang, T.; McWhorter, T. M.; McKeown Wessler, G. C.; Yao, Y.; Song, R.; Mitzi, D. B.; Blum, V. Exploration, Prediction, and Experimental Verification of Structure and Optoelectronic Properties in I_2-Eu-IV-X_4 (I = Li, Cu, Ag; IV = Si, Ge, Sn; X = S, Se) Chalcogenide Semiconductors. *Chem. Mater.* **2024**, *36*, 340–357.

(34)   Yang, Y.; Song, M.; Zhang, J.; Gao, L.; Wu, X.; Wu, K. Coordinated Regulation on Critical Physiochemical Performances Activated from Mixed Tetrahedral Anionic Ligands in New Series of $Sr_6A_4M_4S_{16}$ (A = Ag, Cu; M = Ge, Sn) Nonlinear Optical Materials. *Dalton Trans.* **2020**, *49*, 3388–3392.

(35)   Tampier, M. *Chalkogenogermanate Der Übergangselemente Mit Unedlen Metallen*; Düsseldorf, Germany, 2002.

(36)   Bruker APEX4 Version 2009.5-1 Data Collection and Processing Software; Bruker Analytical X-Ray Instruments, Inc.: Madison, WI, 2009.

(37)   Sheldrick, G. M. SADABS, Bruker AXS, Inc., Madison, Wisconsin, USA, 2008.

(38)   Sheldrick, G. M. XPREP Version 2008/2, Bruker AXS Inc., Madison, 2018.

(39)   Sheldrick, G. M. A Short History of SHELX. *Acta Cryst. A* **2008**, *64* (1), 112–122.

(40)   Sheldrick, G. M. Crystal Structure Refinement with SHELXL. *Acta Cryst. C* **2015**, *71*, 3–8.

(41)   Spek, A. L. Single-Crystal Structure Validation with the Program PLATON. *J. Appl. Cryst.* **2003**, *36*, 7–13.

(42)   Gelato, L. M.; Parthé, E. STRUCTURE TIDY – a Computer Program to Standardize Crystal Structure Data. *J. Appl. Cryst.* **1987**, *20*, 139–143.

(43)   Makuła, P.; Pacia, M.; Macyk, W. How To Correctly Determine the Band Gap Energy of Modified Semiconductor Photocatalysts Based on UV–Vis Spectra. *J. Phys. Chem. Lett.* **2018**, *9*, 6814–6817.

(44)   Kurtz, S. K.; Perry, T. T. A Powder Technique for the Evaluation of Nonlinear Optical Materials. *J. Appl. Phys.* **1968**, *39*, 3798–3813.

(45)   Kresse, G.; Furthmüller, J. Efficient Iterative Schemes for *Ab Initio* Total-Energy Calculations Using a Plane-Wave Basis Set. *Phys. Rev. B* **1996**, *54*, 11169–11186.

(46)   Kresse, G.; Furthmüller, J. Efficiency of Ab-Initio Total Energy Calculations for Metals and Semiconductors Using a Plane-Wave Basis Set. *Comput. Mater. Sci.* **1996**, *6*, 15–50.

(47)   Wessler, G.C.M.; Wang, T.; Blum, V.; Mitzi, D.B. Cubic Crystal Structure Formation and Optical Properties within the Ag-B^{II}-M^{IV}-X (B^{II} = Sr, Pb; M^{IV} =Si, Ge, Sn; X = S, Se) Family of Semiconductors. *Inorg. Chem.* **2022**, *61*, 2929-2944.

(48) Yu, M.; Yang, S.; Wu, C.; Marom, N. Machine Learning the Hubbard *U* Parameter in DFT+*U* Using Bayesian Optimization. *npj Comput. Mater.* **2020**, *6*, 180.

(49)   Hinuma, Y.; Pizzi, G.; Kumagai, Y.; Oba, F.; Tanaka, I. Band Structure Diagram Paths Based on Crystallography. *Comput. Mater. Sci.* **2017**, *128*, 140–184.

(50)   Hobden, M. V. Optical Activity in a Non-Enantiomorphous Crystal: $AgGaS_2$. *Acta Cryst. A* **1968**, *24*, 676–680.

(51)   Lin, Y.-J.; Ye, R.; Yang, L.-Q.; Jiang, X.-M.; Liu, B.-W.; Zeng, H.-Y.; Guo, G.-C. $BaMnSnS_4$ and $BaCdGeS_4$: Infrared Nonlinear Optical Sulfides Containing Highly Distorted Motifs with Centers of Moderate Electronegativity. *Inorg. Chem. Front.* **2019**, *6*, 2365–2368.

(52)   Guo, S.-P.; Chi, W.; Zou, J.-P.; Xue, H.-G. Crystal and Electronic Structures, and Photoluminescence and Photocatalytic Properties of α-$EuZrS_3$. *New J. Chem.* **2016**, *40*, 10219–10226.

(53)   Assoud, A.; Kleinke, H. Unique Barium Selenostannate−Selenide: $Ba_7Sn_3Se_{13}$ (and Its Variants $Ba_7Sn_3Se_{13-\delta}Te_\delta$) with $SnSe_4$ Tetrahedra and Isolated Se Anions. *Chem. Mater.* **2005**, *17*, 4509–4513.

(54)   Yuan, F.-Y.; Lin, C.-S.; Huang, Y.-Z.; Zhang, H.; Zhou, A.-Y.; Chai, G.-L.; Cheng, W.-D. BaCdGeSe$_4$: Synthesis, Structure and Nonlinear Optical Properties. *J. Solid State Chem.* **2021**, *302*, 122352.

(55)   Dou, Y.; Chen, Y.; Li, Z.; Iyer, A. K.; Kang, B.; Yin, W.; Yao, J.; Mar, A. SrCdGeS$_4$ and SrCdGeSe$_4$: Promising Infrared Nonlinear Optical Materials with Congruent-Melting Behavior. *Cryst. Growth Des.* **2019**, *19*, 1206–1214.

(56)   Zhen, N.; Wu, K.; Wang, Y.; Li, Q.; Gao, W.; Hou, D.; Yang, Z.; Jiang, H.; Dong, Y.; Pan, S. BaCdSnS$_4$ and Ba$_3$CdSn$_2$S$_8$: Syntheses, Structures, and Non-Linear Optical and Photoluminescence Properties. *Dalton Trans.* **2016**, *45* (26), 10681–10688.

(57)   Jana, S.; O'Donnell, S.; Leahy, I. A.; Koldemir, A.; Pöttgen, R.; Smaha, R. W.; Maggard, P. A. Synthesis, Crystal Structure, and Physical Properties of the Eu(II)-Based Selenide Semiconductor: EuHfSe$_3$ (Submitted).

(58)   Bera, T. K.; Kanatzidis, M. G. Na$_2$EuAs$_2$S$_5$, NaEuAsS$_4$, and Na$_4$Eu(AsS$_4$)$_2$: Controlling the Valency of Arsenic in Polysulfide Fluxes. *Inorg. Chem.* **2012**, *51*, 4293–4299.

(59)   Mar, A.; Ibers, J. A. Structure of Europium Zirconium Selenide, EuZrSe$_3$. *Acta Cryst. C* **1992**, *48*, 771–773.

(60)   K. Łątka, in: Magnetism and Hyperfine Interactions in Gd*T*$_2$Si$_2$ Systems, Report No1443/PS, Institute of Nuclear Physics, Cracow **1989**, Chapt. 5, p. 68.

(61)   Czjzek, G.; Oestreich, V.; Schmidt, H.; Łątka, K.; Tomala, K. A Study of Compounds GdT$_2$Si$_2$ by Mössbauer Spectroscopy and by Bulk Magnetization Measurements. *J. Magn. Magn. Mater*. **1989**, *79*, 42-56.

(62)   Pöttgen, R.; Johrendt, D. Euiatomic Intermetallic Europium Compounds: Syntheses, Crystal Chemistry, Chemical Bonding, and Physical Properties. *Chem. Mater*. **2000**, *12*, 875-897

(63)   Abudurusuli, A.; Wu, K.; Pan, S. Four New Quaternary Chalcogenides A$_2$Ba$_7$Sn$_4$Q$_{16}$ (A = Li, Na; Q = S, Se): Syntheses, Crystal Structures Determination, Nonlinear Optical Performances Investigation. *New J. Chem.* **2018**, *42*, 3350–3355.

(64) Duan, R.; Lin, H.; Wang, Y.; Zhou, Y.; Wu, L. Non-Centrosymmetric Sufides $A_2Ba_6MnSn_4S_{16}$ (A = Li, Ag): Syntheses, Structures and Properties. *Dalt. Trans.* **2020**, *49*, 5914-5920.

(65) Yu, P.; Zhou, L.-J.; Chen, L. Noncentrosymmetric Inorganic Open-Framework Chalcohalides with Strong Middle IR SHG and Red Emission: $Ba_3AGa_5Se_{10}Cl_2$ (A = Cs, Rb, K). *J. Am. Chem. Soc.* **2012**, *134*, 2227–2235.

(66) Li, Y.-Y.; Liu, P.-F.; Hu, L.; Chen, L.; Lin, H.; Zhou, L.-J.; Wu, L.-M. Strong IR NLO Material $Ba_4MGa_4Se_{10}Cl_2$: Highly Improved Laser Damage Threshold via Dual Ion Substitution Synergy. *Adv. Opt. Mater.* **2015**, *3*, 957–966.

(67) Chung, I.; Malliakas, C. D.; Jang, J. I.; Canlas, C. G.; Weliky, D. P.; Kanatzidis, M. G. Helical Polymer $1/\infty[P_2Se_6^{2-}]$: Strong Second Harmonic Generation Response and Phase-Change Properties of Its K and Rb Salts. *J. Am. Chem. Soc.* **2007**, *129*, 14996–15006.

(68) Lu, B.; Sayyad, S.; Sanchez-Martinez, M.A.; Manna, K.; Felser, C.; Grushin, A.G.; Torchinsky, D.H. Second Harmonic Generation in the Topological Multifold Semimetal RhSi. *Phys. Rev. Research* **2022**, *4*, L022022.